## COMMUNICATION

Check for updates

# Diindolocarbazole – achieving multiresonant thermally activated delayed fluorescence without the need for acceptor units†‡

David Hall, [*ab] Kleitos Stavrou, [c] Eimantas Duda, [d] Andrew Danos, [c] Sergey Bagnich, [d] Stuart Warriner, [e] Alexandra M. Z. Slawin, [a] David Beljonne, [b] Anna Köhler, [*d] Andrew Monkman, [*c] Yoann Olivier [*f] and Eli Zysman-Colman [*a]

In this work we present a new multi-resonance thermally activated delayed fluorescence (MR-TADF) emitter paradigm, demonstrating that the structure need not require the presence of acceptor atoms. Based on an *in silico* design, the compound DiICzMes₄ possesses a red-shifted emission, enhanced photoluminescence quantum yield, and smaller singlet-triplet energy gap, $\Delta E_{ST}$, than the parent indolocarbazole that induces MR-TADF properties. Coupled cluster calculations accurately predict the magnitude of the $\Delta E_{ST}$ when the optimized singlet and triplet geometries are used. Slow yet optically detectable reverse intersystem crossing contributes to low efficiency in organic light-emitting diodes using DiICzMes₄ as the emitter. However, when used as a terminal emitter in combination with a TADF assistant dopant within a hyperfluorescence device architecture, maximum external quantum efficiencies of up to 16.5% were achieved at CIE (0.15, 0.11). This represents one of the bluest hyperfluorescent devices reported to date. Simultaneously, recognising that MR-TADF emitters do not require acceptor atoms reveals an unexplored frontier in materials design, where yet greater performance may yet be discovered.

### New concepts

Thermally activated delayed fluorescence (TADF) compounds have generated tremendous interest over the past decade for use as emitters in organic light-emitting diodes (OLEDs). The conventional donor–acceptor (D–A) design presented in the literature shows broad and unstructured emission, resulting in poor colour purity in the devices. A sub-class of TADF materials, so-called multi-resonant TADF (MR-TADF) overcomes this issue, emitting with very narrow spectra. Compared to D–A TADF materials there are relatively few MR-TADF materials. This is in part due to the poor *in silico* modelling of these compounds. We recently reported how wavefunction-based methods were necessary to accurately model them. We have since exploited this computational methodology towards the design of a number of novel MR-TADF compounds. In previous MR-TADF designs, acceptor atoms or functionalities were essential components in the polycyclic aromatic hydrocarbon compounds to achieve TADF. In the present contribution we demonstrate conclusively that this is not the case and MR-TADF with no acceptor groups is possible. We report a tetramesitylated diindolocarbazole emitter that shows TADF. We further report one of the deepest blue hyperfluorescent OLEDs using this compound as a terminal emitter.

## Introduction

The organic light-emitting diode (OLED) field has taken another step forward with the introduction of multiresonant thermally activated delayed fluorescent (MR-TADF) materials.[1] As with conventional donor–acceptor (D–A) TADF emitters, MR-TADF compounds possess suitably small singlet–triplet energy gaps ($\Delta E_{ST}$) to permit triplet excitons to be up-converted to singlets by reverse intersystem crossing (RISC), unlocking considerably improved device efficiency in OLEDs[2–4] alongside

[a] *Organic Semiconductor Centre, EaStCHEM School of Chemistry, University of St Andrews, St Andrews, KY16 9ST, UK. E-mail: eli.zysman-colman@st-andrews.ac.uk; Web: http://www.zysman-colman.com*

[b] *Laboratory for Chemistry of Novel Materials, University of Mons, 7000, Mons, Belgium*

[c] *Department of Physics, Durham University, Durham, DH1 3LE, UK. E-mail: a.p.monkman@durham.ac.uk*

[d] *Soft Matter Optoelectronics, BIMF & BPI, University of Bayreuth, Universitätsstraße 30, Bayreuth 95447, Germany. E-mail: anna.koehler@uni-bayreuth.de*

[e] *School of Chemistry, University of Leeds, Woodhouse Lane, Leeds, UK*

[f] *Laboratory for Computational Modeling of Functional Materials, Namur Institute of Structured Matter, University of Namur, Rue de Bruxelles, 61, Namur 5000, Belgium. E-mail: yoann.olivier@unamur.be*

applications in several other optoelectronic contexts.[5–8] RISC is achieved in D–A TADF materials through the reduction of the exchange integral by electronically decoupling the donor and acceptor moieties as a result of a highly twisted conformation,[2,4] with the HOMO situated on the donor and LUMO on the acceptor, combined with vibronic coupling between local and charge transfer triplet states to facilitate spin orbit coupling.[9] Due to the conformational flexibility inherent in these classes of emitter, the charge-transfer emission bands are particularly broad, resulting in poor colour purity of the resulting OLEDs and extreme challenges in achieving deep-blue colour coordinates.[10]

For MR-TADF emitters the HOMO–LUMO separation and thus small $\Delta E_{ST}$ are achieved via a complementary pattern of the electron density distribution on adjacent atoms within the molecule[1] between HOMO and LUMO states, made possible by the incorporation of suitably positioned electron-donating and electron-withdrawing atoms (or functional groups). The reorganization of the electron density upon excitation is relatively localized, so that the lowest singlet and triplet excited states possess short-range charge transfer (SRCT) character.[11] The small exchange integral in MR-TADF compounds is best illustrated

with difference density plots (Fig. 1). Seemingly paradoxical for charge-transfer states, there is also a suitably large overlap of the excited and ground state wavefunctions, leading to larger oscillator strengths for the $S_1$–$S_0$ transition and thus fast radiative decay rates, $k_r$. We note that the wavefunction will be of mixed locally excited (LE) and CT character, and in this case the LE contribution appears to dominate, thus coupling to the ground state is high but electron exchange energy remains sizeable. Combined with conformationally rigid structures these SRCT states confer a very narrow emission spectrum with full width at half maxima (FWHM) below 30 nm,[1] leading to much greater colour purity, which is required for high-definition displays and advantageous for achieving deep-blue emission.[12]

MR-TADF materials **DABNA-1** and **DABNA-2** were first reported in 2016 by Hatakeyama and co-workers.[13] These compounds contain a central accepting boron atom and para-disposed donating nitrogen atoms that achieve the desired alternating pattern of the electron density distribution. OLEDs employing **DABNA-1** and **DABNA-2** showed maximum external quantum efficiencies, $EQE_{max}$, of 13.5% and 20.2% with Commission Internationale de l'Éclairage, CIE, coordinates of (0.13, 0.09) and (0.12, 0.13), respectively. Low RISC rates (compared to
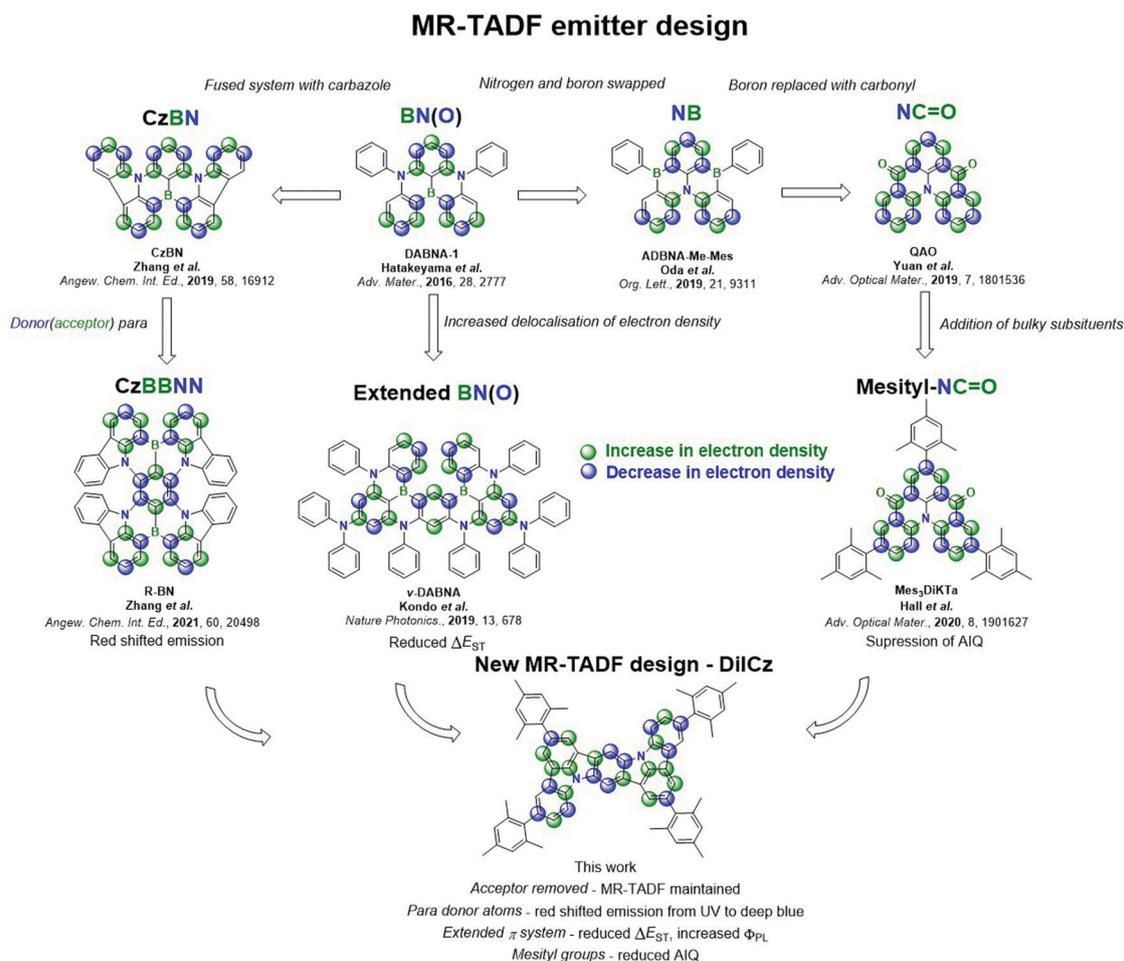


**Fig. 1** Evolution of MR-TADF emitters including simplified difference density plots for each core.

contemporaneous D–A–D emitters)[14–17] in this early work resulted in severe efficiency roll-off though, with efficiencies at 1000 cd m$^{-2}$ not reported. A large number of other MR-TADF materials using this same design template have since been reported.[18–20]

Dramatic improvements in both EQE$_{max}$ and efficiency roll-off were recently reported for the extended system *v*-DABNA (Fig. S1, ESI‡).[21] This compound contains two DABNA-1 units that are fused together, extending the π conjugation (Fig. 1), which results in a smaller $\Delta E_{ST}$ from 0.18 eV in DABNA-1 (in 1 wt% mCBP)[13] to 0.02 eV (in 1 wt% DOBNA-OAr).[21] OLEDs made with this emitter show an outstanding EQE$_{max}$ of 34.4% at CIE (0.12, 0.11), assisted in part by spontaneous emitter alignment improving device optical outcoupling, as confirmed by angularly-resolved emission measurements in a later work.[22] Further, due in part to its small $\Delta E_{ST}$ and class-leading RISC rates, the device shows superior efficiency roll-off, with an EQE at 1000 cd m$^{-2}$ of 26.1% (Table S1, ESI‡).

Another family of MR-TADF compounds, introduced by Zhang *et al.* in 2019,[23] relies on boron and nitrogen atoms to direct the electron density pattern, but these compounds incorporate fused donor units, such as in CzBN. The fused system results in increased electronic delocalisation, thus stabilizing S$_1$, which produces a red-shift in the emission (Fig. 1). The first series of emitters incorporated peripheral electron-withdrawing groups onto the CzBN core, which led to a further red-shift of the emission. OLEDs with 2F-BN, 3F-BN and 4F-BN showed EQE$_{max}$ of 22.0%, 22.7% and 20.9%, respectively, at CIE of (0.16, 0.60), (0.20, 0.58) and (0.12, 0.48), representing the first examples of green-emitting MR-TADF OLEDs. Following this early work a range of materials based on this molecular design have been reported;[23–28] the OLED with BBCz-G showing the highest efficiencies, with an EQE$_{max}$ of 31.8% at CIE of (0.26, 0.68).[29] This design was also used to produce the first examples of red-emitting MR-TADF compounds, BBCz-R[29] and R-(T)BN[30] (Fig. S1, ESI‡). The red-shifted emission in both examples results from the positioning of the donating nitrogen atoms, and thus the withdrawing boron atoms, *para* to each other, thereby inducing partial bonding and antibonding character and resulting in a smaller HOMO–LUMO gap, $\Delta E$, and a much lower energy emissive S$_1$ state.[30] Devices with these three emitters showed EQE$_{max}$ surpassing 20% at CIE coordinates of (0.67, 0.33)[29] and (0.72, 0.18).[30] Another route to colour tuning has been the addition of electron donating and withdrawing substituents on the CzBN core, with blue- or red-shifts of the emission possible depending on the position and number of additional donors and acceptors.[27,29,31,32]

An alternative core unit based on DABNA-1 was presented firstly by Oda *et al.*,[33] where the positions of boron and nitrogen atoms are switched (ADBNA-Me-Mes and ADBNA-Me-Tip, Fig. 1 and Fig. S1, ESI‡). Having two boron and one nitrogen atoms results in a smaller $\Delta E$ compared to that of DABNA-1; however, there is minimal impact on $\Delta E_{ST}$ (Table S1, ESI‡). The resulting OLEDs showed CIE of (0.10, 0.27) and (0.11, 0.29) for ADBNA-Me-Mes and ADBNA-Me-Tip, respectively. The EQE$_{max}$ for these devices are 16.2% and 21.4%, respectively, while efficiency roll-off is modest, with EQE$_{100}$ of 11.2% and 15.4%.

Another family of MR-TADF compounds contains carbonyl groups in lieu of boron atoms as the electron acceptor. The first example, QAO, reported in 2019, translated into devices with an EQE$_{max}$ 19.4% at CIE (0.13, 0.18).[34] We showed that decoration of this core with mesityl groups, Mes$_3$DiKTa, can mitigate aggregation induced quenching (AIQ),[20] which is a common problem with these planar molecules. With this emitter, the OLED showed the highest EQE$_{max}$ for this family of compounds of 21.1% at CIE of (0.12, 0.32). A phenyl-substituted structure, 3MTPTOAT, based on a related core, TOAT, which itself has previously been reported as a room temperature phosphorescent emitter,[35] was used as the emitter in an OLED that showed a very high EQE$_{max}$ of 31.2%.[36] A range of emitters has now been reported incorporating carbonyl groups within the molecular design;[33,34,37] however, most of these emitters show relatively large $\Delta E_{ST}$ and the devices often show EQE$_{max}$ values inferior to 20%. A full summary of the discussed literature emitters including structures, photophysical data and OLED device performances can be found in Fig. S1 and Table S1 (ESI‡).

Despite the excellent characteristics of MR-TADF emitters, the majority of MR-TADF emitters have a low $k_{RISC}$, with most around 10$^4$ s$^{-1}$ (Table S2, ESI‡). The slow $k_{RISC}$ has proved detrimental to device performance with most OLEDs using the MR-TADF compound as an emitter suffering from large efficiency roll-off.[13] In the literature only two examples exist where $k_{RISC}$ surpasses 10$^6$ s$^{-1}$ (Fig. S2, ESI‡), *m*-CzBNCz[27] and BSBS-N1,[38] where $k_{RISC}$ reaches 1.08 and 1.90 × 10$^6$ s$^{-1}$, respectively. Even direct comparison between reported RISC rates from different research teams is challenging though, due to the plurality of reported methods for determining its value[39,40] and subtle yet important practical concerns.[41] The MR-TADF emitters with the fastest $k_{RISC}$ are nevertheless two orders of magnitude slower than the best performing D–A TADF emitter (Fig. S2, ESI‡). This was predicted by Northey and Penfold[42] and experimentally shown by Stavrou *et al.*,[43] that the RISC mechanism in MR-TADF systems occurs through crossing between T$_1$ and an upper triplet state *via* reverse internal conversion. This involves closely-lying triplet states and requires new design rules for new chemical structures with optimal efficiency. A large factor in this apparent gap in RISC rates is that the chemical space explored for MR-TADF emitters remains small compared to the thousands of donor–acceptor TADF compounds reported. Furthermore, we recently demonstrated[11] that time-dependent DFT calculations, which are commonly used to predict the nature and the energies of the excited singlet and triplet states of D–A TADF compounds,[44] do not accurately predict these parameters for MR-TADF compounds, thus hindering computationally guided molecular design. We have shown repeatedly that coupled cluster calculations,[33,45–47] which include double excitation contributions, perform significantly more accurately, albeit at a higher computational cost.

Here, we apply the same coupled cluster methodology to guide the design of a new class of MR-TADF materials, which surprisingly do not require an electron-accepting functionality within the compound. Despite the lack of acceptor atom, a complimentary pattern of increasing and decreasing electron

density is achieved for $S_1$ (but not necessarily for $T_1$) compared to $S_0$ in this class of emitters. **DiICzMes$_4$** was also compared to two smaller reference emitters, **ICz** and **ICzMes$_3$**, with mesityl groups in **DiICzMes$_4$** intended to suppress AIQ.[33] Compared to **ICz** and **ICzMes$_3$**, the expansion of the π-system in **DiICzMes$_4$** ensures a further decrease of the HOMO–LUMO overlap and results in a much smaller $\Delta E_{ST}$, reduced from 0.47 eV in **ICz** to 0.26 eV in **DiICzMes$_4$** (in toluene). Further, there is a desirable increase in $\Phi_{PL}$ across the series from 37%, 56% and 67%, accompanied with a red-shift in the emission maximum, $\lambda_{PL}$, from 374 nm, 387 nm and 441 nm in 3 wt% PMMA films, for **ICz**, **ICzMes$_3$** and **DiICzMes$_4$**, respectively, all in agreement with recent SCS-CC2 calculations for B/N-doped nanographenes.[11]

Crucially, although the core **DiICz** structure decorated with $^t$Bu groups has recently been reported,[48,49] its identity as a TADF emitter – confirmed here by time-resolved photophysical measurements – was overlooked until recently.[50] An analogous non-fused tricarbazole-amine system (**TCA_C4**) had previously been shown to have a small singlet triplet gap, 0.21 eV, and gives moderate TADF *via* a reverse internal conversion (rIC), upper triplet state crossing mechanism.[51] It is only recently that the MR-TADF mechanism has been elucidated to take place through a similar rIC mechanism in **v-DABNA**,[43] and presumably also other MR-TADF emitters. Nonetheless, in both previous reports of the DiICz structure the compound was presented as a purely fluorescent system (named **pICz**[48] and **5**[49]), with relatively large $\Delta E_{ST}$ of 0.29 eV. Recently, a similar derivative, **tPBisICz**, was introduced as a MR-TADF emitter, and the authors contended that RISC proceeds between $T_2$ and $S_1$.[50] The device showed an EQE$_{max}$ of 23.1% at CIE (0.15, 0.05);

however, efficiency roll-off was severe (Table S3, ESI‡) and this is likely due to the inefficient $k_{RISC}$ of $1.4 \times 10^3$ s$^{-1}$. Although the RISC rate for **DiICzMes$_4$** is slow (similar to that of **TCA_C4**[51]), this work supports the existence of an entirely new subcategory of 'acceptor-free' MR-TADFs, which may yield improved performance in device applications in future.

## Results and discussion

### Modelling

Initial ground state optimisation followed by vertical excitation were performed at the SCS-CC2/cc-pVDZ level of theory. Indolocarbazole (**ICz**) has been frequently used by the TADF community, able to act as both a donor or acceptor[52] depending on to the nature of the substituents. $\Delta E_{ST}$ was predicted to be 0.33 eV, which is high for TADF materials but rationalized by the different nature of $S_1$ and $T_1$ excited states. Indeed, $S_1$ displays a typical difference density pattern characteristic of a SRCT excited state while $T_1$ exhibits a locally excited (LE)-like pattern, with the latter more stabilized, hence the large $\Delta E_{ST}$ (Fig. 2). It has been inferred previously that extending the MR-TADF electronic delocalisation could be a viable strategy to decrease $\Delta E_{ST}$ at the same time as increasing the oscillator strength.[11] Based on this hypothesis, four derivatives of **ICz** were modelled, with differing patterns of the relative position of the nitrogen atoms: **DiICz-m-1**, **DiICz-m-2**, **DiICz-p-1** and **DiICz-p-2**. Compared to the parent **ICz**, each of these four emitters has a stabilized $S_1$ state, decreasing from 3.78 eV for **ICz** to 3.58 eV, 3.57 eV, 3.36 eV and 3.32 eV for **DiICz-m-1**,
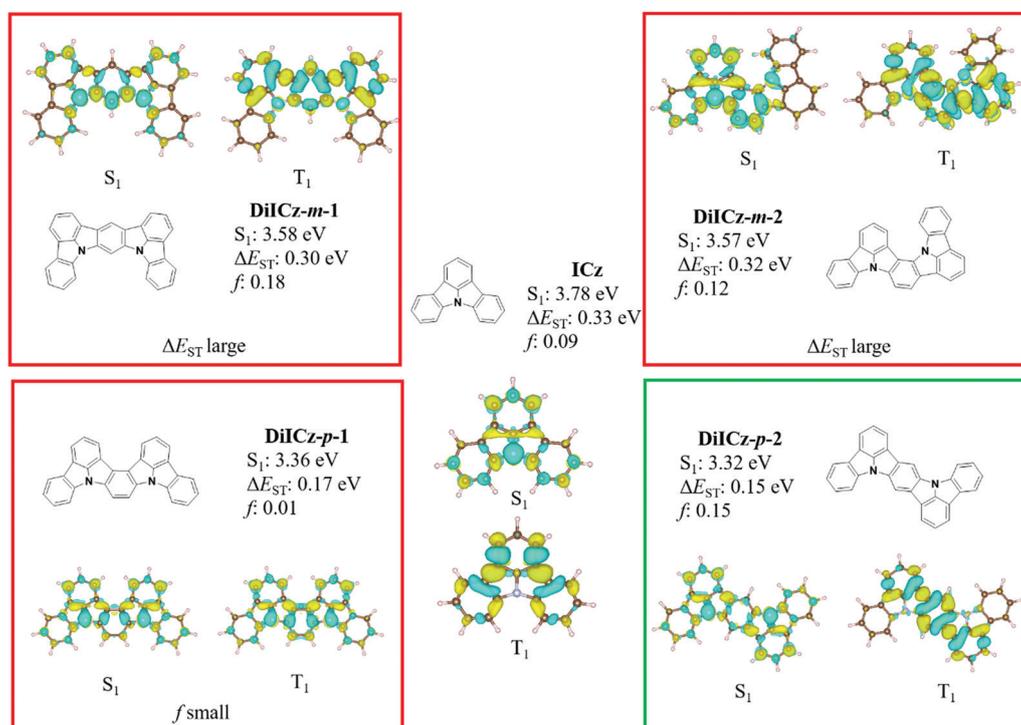


**DiICz-m-1**
$S_1$: 3.58 eV
$\Delta E_{ST}$: 0.30 eV
$f$: 0.18
$\Delta E_{ST}$ large

**DiICz-m-2**
$S_1$: 3.57 eV
$\Delta E_{ST}$: 0.32 eV
$f$: 0.12
$\Delta E_{ST}$ large

**ICz**
$S_1$: 3.78 eV
$\Delta E_{ST}$: 0.33 eV
$f$: 0.09

**DiICz-p-1**
$S_1$: 3.36 eV
$\Delta E_{ST}$: 0.17 eV
$f$: 0.01
$f$ small

**DiICz-p-2**
$S_1$: 3.32 eV
$\Delta E_{ST}$: 0.15 eV
$f$: 0.15

**Fig. 2** $S_1$ and $T_1$ difference density patterns, $\Delta E_{ST}$, $S_1$ energy and oscillator strength, $f$, for the proposed DiICz units.

**DiICz-*m*-2**, **DiICz-*p*-1** and **DiICz-*p*-2**, respectively, the result of delocalization of the $S_1$ wavefunction (see Fig. 2). As previously reported for other MR-TADF emitters,[30] when the donating nitrogen atoms are located *para* to each other the red-shift is the largest. The *para*-derivatives here also have the smallest predicted $\Delta E_{ST}$ of 0.17 eV and 0.15 eV for **DiICz-*p*-1** and **DiICz-*p*-2**, respectively, while $\Delta E_{ST}$ is 0.30 eV and 0.32 eV for **DiICz-*m*-1** and **DiICz-*m*-2**.

Of **DiICz-*p*-1** and **DiICz-*p*-2**, **DiICz-*p*-2** has a considerably larger oscillator strength of 0.15 compared to 0.01 in **DiICz-*p*-1** and thus this motif was assessed as the most promising. Furthermore, we have previously demonstrated that addition of mesityl groups can mitigate AIQ,[33] which plagues MR-TADF materials[43] (and many other similar systems[53,54]) owing to their planar and electron-rich geometries. With this in mind, we designed the mesityl derivative of **ICz**, **ICzMes₃**. In this compound the mesityl groups have the added benefit of reducing $\Delta E_{ST}$ (calculated for vertical transitions from the ground state geometry) from 0.33 eV to 0.21 eV. The decrease in $\Delta E_{ST}$ is essentially the result of preferential stabilization of $S_1$ while the energy of $T_1$ energy is only minimally affected (Fig. S31, ESI‡). The small stabilization of $T_1$ in **ICzMes₃** can be explained by the absence of significant orbital contributions from the carbon atoms connecting the mesityl groups in the $T_1$ difference density pattern (Fig. S31, ESI‡). We also investigated the role that decoration with mesityl groups would play on the core structure of **DiICz-*p*-2**, which together form the target material **DiICzMes₄**. In **DiICzMes₄** (Fig. S31, ESI‡); the mesityl substitution helps to reduce the predicted $\Delta E_{ST}$ from 0.15 eV to 0.13 eV for similar reasons as described for **ICzMes₃**. Due to the close energy of the LE $T_1$ and the SCRT $T_2$ states of the **DiICz-*p*-2**, substitution by the four mesityl groups allows inversion between the two. $T_1$ becomes SCRT in **DiICzMes₄** possessing similar, yet slightly different character than $S_1$. The literature emitter **tBisICz** was also modelled using the same approach and the $\Delta E_{ST}$ of 0.14 eV was found to be larger. Further, the energy gap between $S_1$ and $T_2$ is also larger at 0.07 eV compared to 0.05 eV in **DiICzMes₄**. Owing to these moderate differences in the energy landscape of the excited states, **DiICzMes₄** is expected to show improved RISC rates.

In contrast to previously investigated MR-TADF emitters, we see large changes when comparing $\Delta E_{ST}$ computed from vertical excitation from the ground state geometry and experiments due to the different nature of $T_1$ and $S_1$ states (see difference density plots in Fig. S29 and S30, ESI‡). In such a case, relaxation of the excited states could be key to reach quantitative agreement with the experiments. We thus optimized both the $S_1$ and $T_1$ states within the TDA using PBE0 functional and 6-31G(d,p) basis set, and computed the $T_1$ and $S_1$ excited state energies at the SCS-CC2/cc-PVDZ level of theory for **ICz**, **ICzMes₃** and **DiICzMes₄** as well as for three literature MR-TADF compounds, **DABNA-1**, **BCzBN** and **DiKTa**. Quantitative agreement with the experiments is reached with $\Delta E_{ST}$ increasing for **ICz**, **ICzMes₃** and **DiICzMes₄**, to 0.59 eV, 0.45 eV and 0.29 eV (Fig. 3), respectively, caused by a larger relaxation energy of the $T_1$ state in line with a greater LE character for this state (Tables S9–S11, ESI‡).

Interestingly, such an increase in $\Delta E_{ST}$ does not manifest for **DABNA-1**, **BCzBN** and **DiKTa**, wherein $\Delta E_{ST}$ is only shifted by a maximum of 0.04 eV, owing to the similar SRCT nature of $T_1$ and $S_1$ (see Tables S9–S11 and Fig. S30 and S32, ESI‡). The similar orbital character of $S_1$ and $T_1$ in many previous emitters, and the ones presented here, implies that RISC between these two states is not symmetry allowed according to El Sayed's rules.[9] Thus, RISC must occur *via* a spin-vibronic mechanism involving intermediate triplet states lying between $S_1$ and $T_1$. Irrespective of the starting geometry, a close lying triplet state of different orbital type is present, whose involvement has been shown to contribute to the MR-TADF RISC mechanism.[43] Both smaller $\Delta E_{ST}$ and $\Delta E_{T2T1}$ were observed, decreasing across the series from **ICz**, **ICzMes₃** and **DiICzMes₄**. We observed again a decreased $\Delta E_{ST}$ upon incorporation of mesityl groups from 0.59 eV for **ICz** to 0.45 eV **ICzMes₃**. Unlike previously reported MR-TADF emitters that contain acceptor atoms/groups, for this class it is essential to optimise the excited states in order to achieve quantitative agreement with experimental $\Delta E_{ST}$.

### Synthesis

The materials were synthesised through a multistep reaction sequence outlined in Fig. 4. Carbazole was coupled to 2-bromofluorobenzene under $S_{NAr}$ conditions at elevated temperatures in an excellent yield of 96%. Intramolecular oxidative ring closing using Pd(OAc)₂ afforded **ICz** in a good yield of 85%. Subsequent electrophilic bromination using NBS afforded intermediate **ICzBr₃** in 79% yield, which was then decorated with mesityl groups using a Suzuki–Miyaura coupling reaction, producing **ICzMes₃** in a good yield of 69%. A similar Suzuki–Miyaura coupling was employed to obtain CzMes₂ from dibromocarbazole in 62% following a literature procedure.[55] Intermediate **2** was obtained in 75% *via* an $S_{NAr}$ reaction that proceeded at lower temperature (50 °C). Double oxidative cyclization using Pd(OAc)₂ generated **DiICzMes₄** in 59% yields. Crystals of **ICzMes₃** and **DiICzMes₄** were grown from slow evaporation of methanol into a saturated solution of toluene over several days. Packing in **ICzMes₃** is primarily governed by π–π stacking interactions between mesityl groups on adjacent molecules (Fig. S25, ESI‡). For **DiICzMes₄** π–π stacking occurs between the mesityl group of one molecule and the DiICz core of an adjacent molecule. The ICz unit in both compounds was not perfectly flat (Fig. 4). Thermogravimetric analysis (TGA) of **ICzMes₃** and **DiICzMes₄** (Fig. S24, ESI‡) reveals good thermal stability for both compounds with $T_d$, the temperature representing 5% weight loss, of, respectively, 374 °C and 450 °C.

### Optoelectronic characterization

The electrochemical properties were investigated using cyclic voltammetry (CV) and differential pulse voltammetry (DPV) in DCM for oxidation and DMF for reduction (Fig. 5a), with the electrochemical potentials reported *versus* SCE (Table 1). **ICz** showed irreversible oxidation and reduction waves with the former appearing to undergo polymerisation, which has been previously reported for **ICz**[56] and seen in other carbazole-containing emitters.[57] Addition of the mesityl groups in **ICzMes₃**
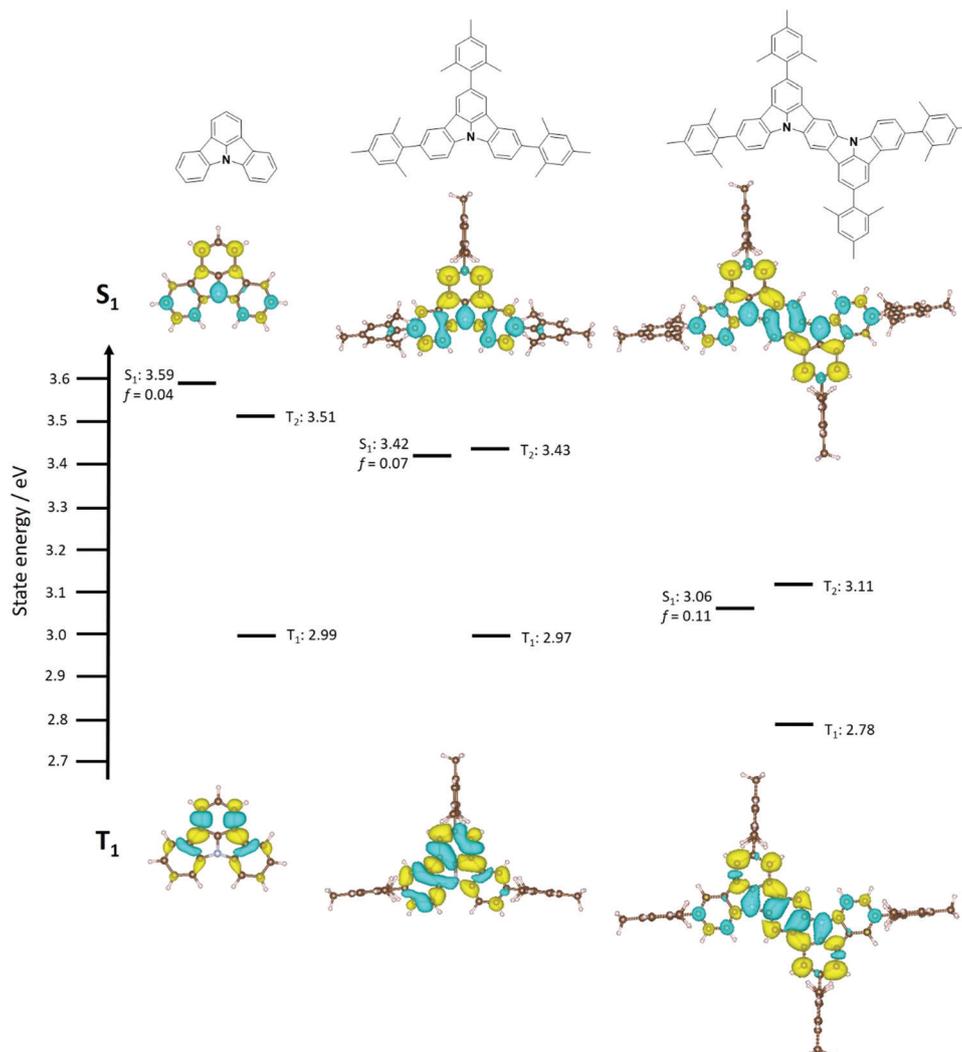
**Fig. 3** Structures, excited state energies and difference density plots of each $S_1$ and $T_1$ for **ICz** (left panel), **ICzMes$_3$** (central panel) and **DiICzMes$_4$** (right panel) from excited state optimized geometry.

renders the oxidation pseudoreversible in a similar manner to what was previously observed for **Mes$_3$DiKTa**,[33] with $E^{ox}$ at 1.45 V versus 1.43 V for **ICzMes$_3$**. Indeed, McNab et al. had demonstrated that the electrochemical instability of **ICz** is associated with dimer formation centred at the *para* positions.[56] There is likewise little change in the irreversible reduction waves with reduction potentials of these two compounds, $E^{red}$, at −2.21 V and −2.16 V for **ICz** and **ICzMes$_3$**, respectively. By contrast, both oxidation and reduction waves for **DiICzMes$_4$** are largely reversible. The oxidation wave is cathodically shifted to 1.11 V while the reduction wave is anodically shifted to −1.92 V, both a reflection of the larger conjugation length of this molecule compared to **ICz** and **ICzMes$_3$**. This produced a significant reduction in the redox gap, $\Delta E_{redox}$, in agreement with calculations, where the calculated $\Delta E$ decreases from 4.65 eV and 4.50 eV for **ICz** and **ICzMes$_3$** to 3.86 eV in **DiICzMes$_4$**. The trends in HOMO and LUMO values are corroborated at the DFT level (Tables S5 and S12, ESI‡).

We next investigated the photophysical properties of the three emitters in solution. The UV-Vis absorption data in toluene (PhMe), 2-methyltetrahydrofuran (2-MeTHF), ethyl acetate (EtOAc), dichloromethane (DCM) and dimethylformamide (DMF) can be found in Fig. S33 and Tables S13–S15 (ESI‡). The polarity of the solvent had minimal impact on the absorption spectra, with nearly identical absorption maxima, $\lambda_{abs}$, and molar absorptivity values, $\varepsilon$, regardless of solvent. Using the representative data in toluene (Table 1), there is a high intensity, low energy band at 364 nm, 379 nm and 431 nm for **ICz**, **ICzMes$_3$**, and **DiICzMes$_4$**, respectively, assigned by calculations to a SRCT band; there is a second distinguishable band at smaller $\varepsilon$ at 350 nm, 363 nm and 410 nm, respectively, that is likely due to a transition to a different vibronic level of the $S_1$ state based on the ca. 0.15 eV energy gap between these two bands. Both **ICz** and **ICzMes$_3$** possess higher energy bands at 320 nm and 330 nm of similar $\varepsilon$, which we assign to transitions to the $S_2$ state. The similar $\varepsilon$ values are captured at the SCS-CC2 level where both $S_1$ and $S_2$ have similar oscillator strengths, $f$, of 0.10 and 0.09 for **ICz** and 0.14 and 0.13 for **ICzMes$_3$**. A far greater oscillator strength of 0.66 is predicted for the transition to $S_2$ for **DiICzMes$_4$** compared to
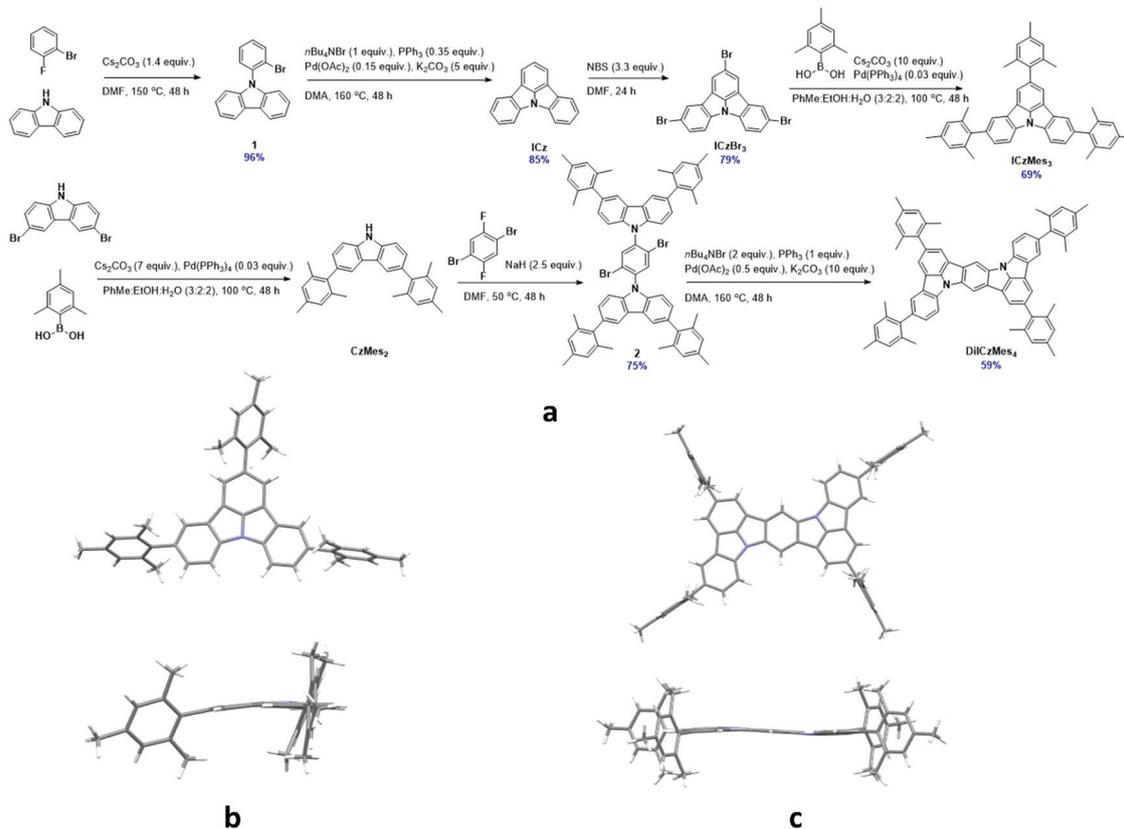
Fig. 4  Synthesis of (a) the emitters and crystal structures of (b) **ICzMes₃** and (c) **DiICzMes₄**.
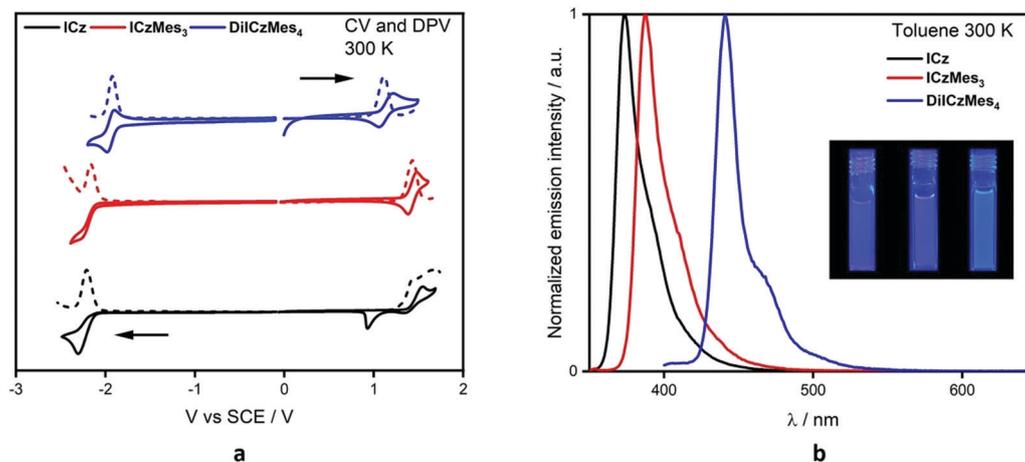


Fig. 5  Solution-state optoelectronic data. (a) CV (solid line) and DPV (dashed) where the anodic scan is in DCM and the cathodic scan is in DMF, with 0.1 M [$n$Bu₄N]PF₆ as the supporting electrolyte and Fc/Fc⁺ as the internal reference (0.46 V for DCM and 0.45 for DMF $vs.$ SCE);[58] (b) steady-state PL in toluene, at concentrations of 0.6–2.0 ×10⁻⁵ M, where $\lambda_{exc}$ = 320 nm for **ICz** and **ICzMes₃** and $\lambda_{exc}$ = 380 nm for **DiICzMes₄**, and pictures of each in solution (**ICz**, **ICzMes₃** and **DiICzMes₄** left to right).

that to S₁ ($f$ = 0.21). Indeed, the band at 365 nm possesses a significantly larger $\varepsilon$ of 39 × 10⁴ M⁻¹ cm⁻¹ compared to that at 431 nm ($\varepsilon$ = 11 × 10⁴ M⁻¹ cm⁻¹), suggesting a greater degree of LE character for the transition associated with this band.

Minimal changes in emission energy and band shape were observed upon modulation of the solvent polarity (Fig. S33 and Tables S13–S15, ESI‡). Such behaviour is characteristic of

MR-TADF emitters, which undergo emission from a SRCT excited state.[11] Owing to their rigid nature, the emission is narrow and the Stokes shifts are small (10, 8, and 10 nm, respectively, for **ICz**, **ICzMes₃** and **DiICzMes₄**) reflecting the very small reorganisation energy between the ground and excited state. The corresponding FWHM for the PL spectra in toluene are 21 nm, 21 nm and 17 nm for **ICz**, **ICzMes₃** and **DiICzMes₄**, respectively. There are

Table 1  Solution optoelectronic data of each emitter

| Compound | $\lambda_{abs}$ $(\varepsilon)^a$/nm ($\times 10^4$ M$^{-1}$ cm$^{-1}$) | $\lambda_{PL}^{a,b}$ (FWHM)/nm | $\Phi_{PL}^c$ N$_2$ (air)/% | S$_1^d$/eV | T$_1^d$/eV | $\Delta E_{ST}^e$/ eV | $\tau_p^f$/ns | HOMO$^g$/ eV | LUMO$^g$/ eV |
|---|---|---|---|---|---|---|---|---|---|
| ICz | 285 (31), 392 (10), 309 (6), 320 (7), 350 (6), 364 (9) | 374 (21)$^h$ | 58 (30) | 3.35 | 2.88 | 0.47 | 15 | −5.79 | −2.14 |
| ICzMes$_3$ | 291 (40), 300 (14), 318 (6), 330 (8), 363 (6), 379 (8) | 387 (21)$^h$ | 66 (43) | 3.24 | 2.85 | 0.39 | 22 | −5.77 | −2.19 |
| DiICzMes$_4$ | 302 (58), 307 (62), 316 (59), 345 (19), 365 (39), 410 (8), 431 (11) | 441 (17)$^i$ | 70 (47)$^j$ | 2.83$^k$ | 2.57$^k$ | 0.26 | 41 | −5.45 | −2.43 |

$^a$ Toluene at 300 K. $^b$ Values in parentheses are the FWHM. $^c$ In degassed toluene measured with an integrating sphere under N$_2$, values in parentheses are in air-saturated solution, $\lambda_{exc}$ = 330 nm. $^d$ From the onset of the steady-state emission and phosphorescence in toluene glass at 77 K, $\lambda_{exc}$ = 330 nm. $^e$ Energy difference between the onset of the steady-state and phosphorescence at 77 K. $^f$ $\lambda_{exc}$ = 355 nm. $^g$ The HOMO and LUMO energies were determined according to $E_{HOMO/LUMO}$ = −($E_{onset}^{ox}$/$E_{onset}^{red}$ + 4.8) eV.[59] $^h$ $\lambda_{exc}$ = 320 nm. $^i$ $\lambda_{exc}$ = 380 nm. $^j$ $\lambda_{exc}$ = 350 nm. $^k$ $\lambda_{exc}$ = 350 nm.

low energy shoulders apparent in the steady-state PL of all three emitters. This shoulder is assigned to a vibronic shoulder (*vide infra*) (Fig. S34, ESI‡).

The energies of the singlet and triplet states, and hence, $\Delta E_{ST}$, were determined based on the high-energy onset of the prompt fluorescence and phosphorescence spectra obtained at 77 K in toluene glass (Fig. S34, ESI‡). In all cases, the phosphorescence is very well vibrationally structured and characteristic of a carbazole moiety in strong contrast with respect to the fluorescence, supporting the different nature of the S$_1$ and T$_1$ excited states. There is a progressive decrease in $\Delta E_{ST}$ of 0.47 eV, 0.39 eV and 0.26 eV for ICz, ICzMes$_3$ to DiICzMes$_4$, respectively, a trend that is well reproduced by the SCS-CC2 calculations when considering the optimized excited state structures (Table S11, ESI‡). We simulated the vibronically resolved fluorescence and phosphorescence spectra for DiCz-*p*-2 (we omitted the mesityl groups from DiICzMes$_4$ to avoid spurious negative vibration modes) and obtain excellent agreement with the corresponding experimental spectra of DiICzMes$_4$ (see Fig. S35, ESI‡). The lower energy shoulder of the fluorescence spectrum observed experimentally is attributed to a vibronic transition based on the cross-comparison with the simulated one. This shoulder disappears with increasing concentration when aggregate emission begins to contribute significantly to the emission spectrum (Fig. S37d, ESI‡). Furthermore, the simulated vibronically-resolved phosphorescence spectrum is also in excellent agreement with the experiment. Interestingly, there is an enhanced vibronic intensity associated with high-frequency (1200–1600 cm$^{-1}$) vibrations in the phosphorescence spectrum in comparison to fluorescence spectrum. This reflects the more pronounced geometric relaxation taking place in T$_1$ compared so S$_1$, which translates into a larger adiabatic $\Delta E_{ST}$ in comparison to the vertical $\Delta E_{ST}$ (Table S11, ESI‡) and provides clear spectroscopic evidence for the different character of the S$_1$ and T$_1$ excited states. This behaviour is again in strong contrast with most of the MR-TADF emitters previously reported in the literature.

The solution photoluminescence quantum yields increase from 58%, 66% and 70% for ICz, ICzMes$_3$ to DiICzMes$_4$, respectively, again reflecting expected trends in the calculations.[11] Time-resolved PL decays revealed prompt CT lifetimes of 15.0 ns, 21.6 ns and 40.5 ns for ICz, ICzMes$_3$ and DiICzMes$_4$, respectively. A small contribution of delayed emission was observed for ICz, which was ascribed to originate from TTA (Fig. S34b, ESI‡), while no delayed emission was observed for either ICzMes$_3$ or DiICzMes$_4$ (Fig. S34d and f, ESI‡).

We next investigated the solid-state PL behaviour in a wide bandgap host, PMMA at 3 wt% doping of emitter. This and subsequent wide bandgap (high triplet energy) OLED hosts were selected to strongly exclude the possibility of guest-to-host triplet quenching in both optical and device investigations. The $\lambda_{PL}$ are 377 nm, 391 nm and 442 nm for ICz, ICzMes$_3$ and DiICzMes$_4$, respectively, values that are modestly red-shifted compared to those in toluene. The $\Delta E_{ST}$ values are similar to those measured in toluene at 0.50 eV, 0.41 eV and 0.29 eV for ICz, ICzMes$_3$ and DiICzMes$_4$, respectively, and align with the calculated $\Delta E_{ST}$ using optimized excited state structures. The $\Phi_{PL}$ are similar to those in toluene at 37%, 58% and 67%, for ICz, ICzMes$_3$ and DiICzMes$_4$, respectively. Again, a red-shifted emission, a decreased $\Delta E_{ST}$ and an improved $\Phi_{PL}$ are observed across the series from ICz to ICzMes$_3$ and to DiICzMes$_4$ (Fig. S34, ESI‡). Owing to their large $\Delta E_{ST}$ and excessive S$_1$ energies, the photophysical properties of ICz and ICzMes$_3$ were not investigated in other hosts.

We next investigated the photophysical properties of DiICzMes$_4$ in mCP as this OLED-compatible host matrix has a suitably large T$_1$ energy of 2.9 eV.[60] The optimum doping concentration as a function of $\Phi_{PL}$ was determined (Fig. 6a and Table S16, ESI‡). No AIQ was observed up to 3 wt%, with $\Phi_{PL}$ maintained at 82%; beyond this concentration the $\Phi_{PL}$ decreases, with neat films showing a $\Phi_{PL}$ of 30% (Fig. 6a). The FWHM of a drop-cast 3 wt% doped film in mCP is larger at 40 nm; a low-energy shoulder increases in intensity with increasing doping, which we assigned to an emission from an aggregate (Fig. S37d, ESI‡). However, when films were spin-coated, the aggregate formation could be suppressed, with 3 wt% spin-coated films having a FWHM of 21 nm at $\lambda_{PL}$ 451 nm. At this concentration the $\Delta E_{ST}$ is 0.26 eV, leading to a long $\tau_d$ of 433 μs but with a delayed emission suppressed at low temperatures (Fig. 6c). A similar behaviour exists when DiICzMes$_4$ is doped in DPEPO at 5 wt% where the delayed emission is no longer observed below 80 K (Fig. S38b, ESI‡). In the time-resolved measurements the spectra of the delayed emission match that of the prompt fluorescence, and thus can be assigned to emission from the S$_1$ state rather than any room temperature phosphorescence, which has been observed in other rigid systems[61] (Fig. S37b, ESI‡). TTA was ruled out as the emission mechanism owing to the linear power dependence of the emission intensity (Fig. 6d).[62]
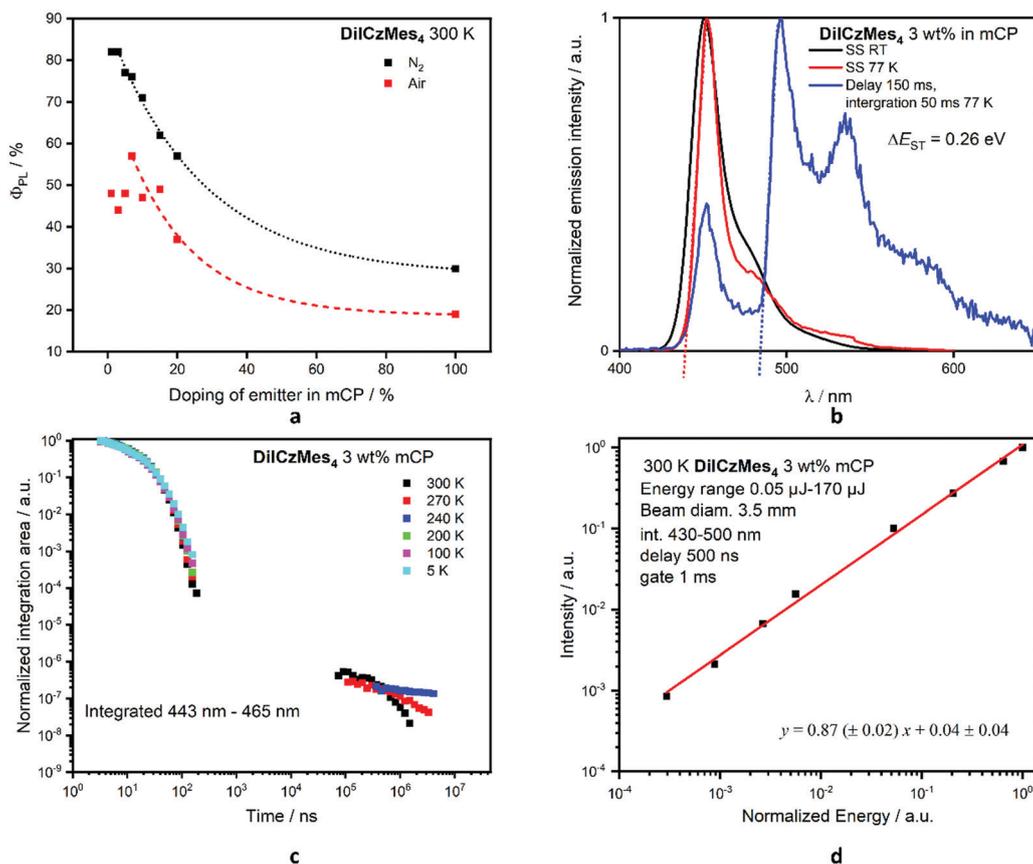
**Fig. 6** Solid-state photophysics of **DiICzMes₄**. (a) $\Phi_{PL}$ as a function of doping concentration, calculated using an integrating sphere. An exponential decay has been fitted to guide the reader, $\lambda_{exc} = 350$ nm; (b) steady-state (SS) emission spectra at RT ($\lambda_{exc} = 330$ nm) and 77 K and phosphorescence spectrum at 77 K in 3 wt% mCP films, ($\lambda_{exc} = 350$ nm); (c) temperature-dependent time-resolved PL decays in 3 wt% mCP films, $\lambda_{exc} = 355$ nm; (d) intensity dependence as a function of laser power in 3 wt% mCP, $\lambda_{exc} = 355$ nm.

The contribution of the delayed emission to the overall emission is often small in MR-TADF emitters, reflecting the efficient $k_r^S$ (and small $\Phi_{ISC}$) and the slow $k_{RISC}$. For instance, for **DABNA-1** and **DiKTa** the $\Phi_d$ is around 4% for 1 wt% **DABNA-1**[13] in mCBP and 1% for **DiKTa** in toluene.[33] For **DiICzMes₄**, the $\Phi_d$ is 1.2%, and thus $k_{RISC}$ is slow in this emitter, at $1.8 \times 10^2$ s$^{-1}$ following the methodology of Masui *et al.*[63] This is substantially slower than most MR-TADF emitters, but similar to **tPBisICz** and **tBisICz**, which were reported as 1.4 and $0.14 \times 10^3$ s$^{-1}$, respectively, in 1 wt% mCP:TSPO1 films.[50] In this work, neither **ICz** nor **ICzMes₃** show TADF due to their too large $\Delta E_{ST}$ of 0.47 eV and 0.39 eV, respectively, measured in toluene glass; however, **DiICzMes₄** shows weak (though unambiguous) TADF as its $\Delta E_{ST}$ of 0.26 eV is much smaller (Table 2).

In anticipation of OLED applications, additional time-resolved emission decays were also collected for **DiICzMes₄** in a wide range of suitably high-triplet OLED hosts (Fig. S38, ESI‡). For these experiments 10% loading in drop-cast films was used, improving the overall signal but also enhancing the emission detectable from red-shifted dimer or excimer species, as evident in the individual normalised spectra (contour plots, Fig. S38c, ESI‡). In line with the stationary emission spectra of MR-TADF materials in varying solvent polarity (Fig. S33, ESI‡),

**Table 2** Solid-state photophysical properties

| Compound[a] | $\lambda_{PL}$ (FWHM)[b]/ nm | $\Phi_{PL}$[c]/ % | $S_1$[d]/ eV | $T_1$[d]/ eV | $\Delta E_{ST}$[e]/ eV | $\tau_p$[f]/ ns | $\tau_d$[f]/ μs |
|---|---|---|---|---|---|---|---|
| **ICz** | 377 (29) | 37 | 3.38 | 2.88 | 0.50 | N/A | N/A |
| **ICzMes₃** | 391 (28) | 58 | 3.26 | 2.85 | 0.41 | N/A | N/A |
| **DiICzMes₄** | 442 (20)[g] | 67 | 2.86[h] | 2.57[h] | 0.29 | N/A | N/A |
| **DiICzMes₄**[i] | 451 (22)[g] | 82[f] | 2.82[h] | 2.56[h] | 0.26 | 14 | 433 |

[a] In 3 wt% doped PMMA films. [b] $\lambda_{exc} = 330$ nm, where value in parentheses is FWHM. [c] Determined using an integrating sphere, $\lambda_{exc} = 330$ nm. [d] $S_1$ and $T_1$ determined from the onset of the steady-state and phosphorescence spectra, respectively, at 77 K, $\lambda_{exc} = 330$ nm. [e] Calculated from the energy difference between the energies of the $S_1$ and $T_1$ states at 77 K. [f] $\lambda_{exc} = 355$ nm. [g] $\lambda_{exc} = 350$ nm. [h] $\lambda_{exc} = 350$ nm. [i] In 3 wt% doped mCP films.

we observe only minor differences in the time-resolved spectra and decays regardless of host.

**Devices**

Regioisomeric derivatives of DiICz have been reported in the form of **4**,[49] ***m*-FLDID**[64] and **tDIDCz**,[65] where each was described as a traditional fluorescent emitter. Large experimentally determined $\Delta E_{ST}$ values of 0.36 eV and 0.44 eV were reported for ***m*-FLDID**[64] and **tDIDCz**,[65] respectively, in frozen
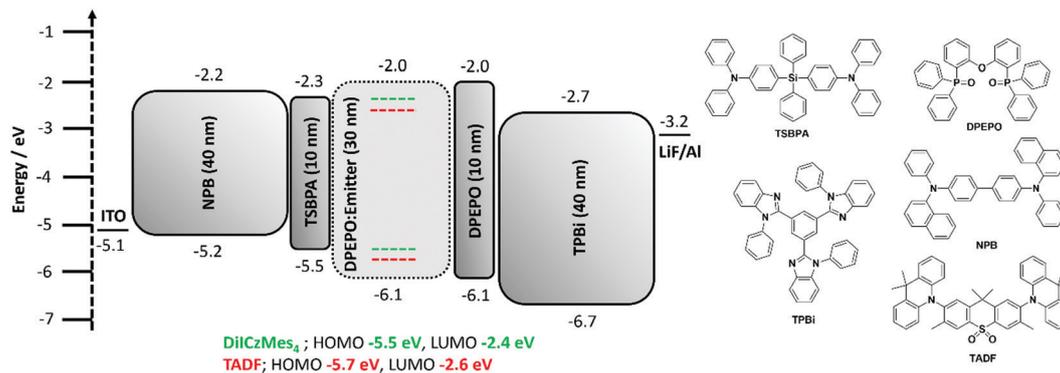
**Fig. 7** Device architecture and chemical structures of materials employed.

THF glass. The corresponding UV-emitting OLEDs showed $EQE_{max}$ of 5.2% and 3.3% at CIE of (0.16, 0.03) and (0.16, 0.02), respectively. Having confirmed the previously overlooked though admittedly weak TADF activity of **DiICzMes₄**, its use as an emitter in OLEDs was assessed. Devices using a stack of ITO (HIL/anode) |NPB (HTL, 40 nm)|TSBPA (EBL, 10 nm)|**DiICz-Mes₄**:DPEPO 10% (EML, 30 nm)|DPEPO (HBL, 10 nm)|TBPi (ETL, 40 nm)|LiF (EIL, 1 nm)|Al (cathode, 100 nm) were fabricated (Fig. 7), with representative performance shown

in Fig. 8. These results show that the low rate of RISC in **DiICzMes₄** is insufficient to enable efficient triplet harvesting even at the lowest current densities (and corresponding lowest brightness, $\sim 10$ cd m$^{-2}$) investigated here. The resulting low $EQE_{max}$ values are consistent with the **DiICzMes₄** acting akin to a fluorescent dopant, only able to harvest singlet excitons for emission with an upper limit of $EQE_{max} < 5\%$. This result is in-line with what was observed for previous acceptor-free rIC DF material **TCA_C4**.[51] The OLED shows CIE coordinates of
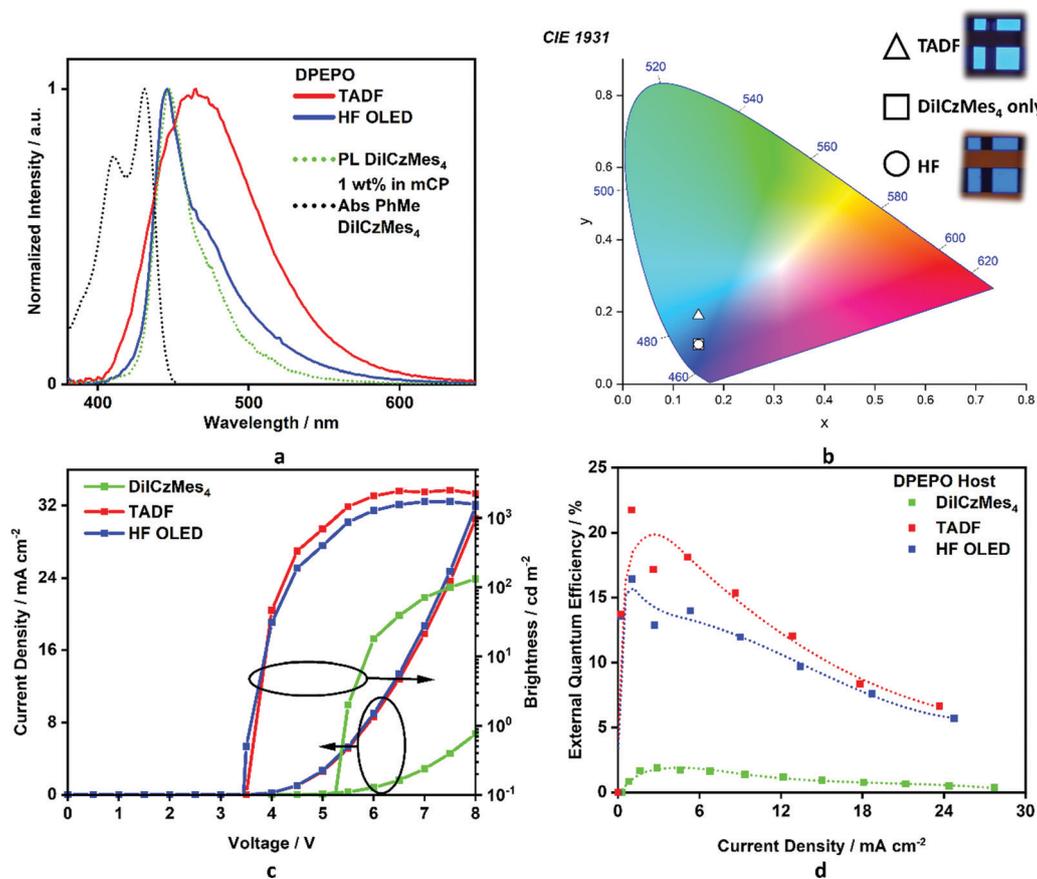


**Fig. 8** OLED performance for different EMLs. (a) EL spectra of TADF D−A−D 35% (red), HF OLEDs 1:35 wt% (blue) in DPEPO host, absorption (black dotted) and PL (green) spectra of **DiICzMes₄** 1 wt% in mCP for comparison. (b) CIE coordinates, where square (**DiICzMes₄** only) and circle (HF) overlap, (c) *JVL* curves, and (d) EQE *vs.* current density, where fitting has been applied (dotted line) to guide the reader.

(0.15, 0.11). Despite the higher EQE$_{max}$ observed for **tPBisICz** at very low brightnesses, the efficiency roll-off of that device was severe with the EQE at 100 cd m$^{-2}$ only about 5%. Comparing our OLED results at equivalent brightnesses reveals similar overall performance metrics with the previously reported work (Table S3, ESI‡).[50]

Additional devices using a different stack consisting of ITO|NPB (HTL, 40 nm)|mCBP (EBL, 10 nm)|**DiICzMes$_4$**:host X% (EML, 30 nm)|T2T (HBL, 10 nm)|T2T:LiQ 45% (EIL/ETL, 35 nm)|Al (cathode, 100 nm) were also fabricated. In these the concentration of the dopant was varied (5, 12, and 20 wt%) and different EML hosts additionally investigated: mCBP (hole transporting), DPEPO (electron transporting). Representative device performance and spectra are shown in Fig. S39 (ESI‡), with no significant improvement compared to the results in Fig. 8. With increasing concentration no difference was observed in current density–voltage–luminance (*JVL*) and EQE as a function of current density although a broadening in the electroluminescence (EL) spectrum was observed. The broadening is assigned to the dimer/excimer contribution as shown from the previous photophysical results (Fig. S37d and S38c, ESI‡).

In order to compensate for the low RISC rate of **DiICzMes$_4$** we also applied it as a terminal emitter in hyperfluorescent OLEDs (HF OLEDs) with a D–A–D TADF co-host. In order to ensure good spectral overlap necessary for energy transfer, we employed a dimethylacridine-tetramethylthioxanthene-*S*,*S*-dioxide (identified as TADF in Fig. 7) based TADF previously reported to give high EQEs and blue emission [CIE of (0.15, 0.19)] in the same OLED stack.[14] This D–A–D TADF was co-evaporated at 35% in the EML, alongside 1% **DiICzMes$_4$** and bulk host DPEPO. The resulting OLEDs possessed good efficiency, with an EQE$_{max}$ > 16% and CIE of (0.15, 0.11) enabled by triplet harvesting of the D–A–D co-host, while outputting narrow blue emission from the **DiICzMes$_4$**. The HF OLED showed relatively lower efficiency roll-off, offering a practical strategy to circumvent large efficiency roll-off resulting from inefficient $k_{RISC}$ of the MR-TADF emitter (Fig. 8).

As our integrating sphere system is not sensitive to very low luminances, we do not observe the same high maximum EQEs (∼32%) previously reported using a similar hyperfluorescence approach with **pICz**.[48] However, comparing our device data at equivalent brightnesses reveals improved performance (Fig. S40, ESI‡), which we infer is due to the improved efficiency roll-off of our D–A–D co-host. Indeed, this performance at higher brightnesses is amongst some of the best reported for HF OLEDs at this colour coordinate (Table S18, ESI‡). The previously reported **DPAc-DtCzBN**:PPF co-host has a similar intrinsic maximum efficiency as ours, and with slightly blue shifted EL spectrum should also enjoy marginally improved FRET overlap with the MR-TADF emitter in the device. Despite the adequate FRET overlap in both devices, a subtle shoulder can still be observed in our EL spectra, indicating residual emission from the D–A–D co-host. As hyperfluorescence applications of MR-TADF emitters become increasingly popular to circumvent their low RISC rates,[22,66–68] engineering both their PL spectra (for ideal-blue emission), as well as their absorption spectra (for minimal Stokes shift, enabling broad compatibility with D–A–D TADF co-hosts)[69] take on equally important roles

for applications. The latter of these can significantly alleviate the requirement for D–A–D co-hosts with deep blue EL, which remain challenging to design despite nearly a decade of intense global research in this direction.

We finally note that in both our hyperfluorescence devices and those previously reported, inclusion of the MR-TADF leads to significantly worse efficiencies at reasonable brightnesses compared to the D–A–D co-host alone. While the **DiICzMes$_4$** would be expected to increase device performance due to spontaneously emitter dipole alignment and improved outcoupling,[48] other detrimental processes must also be at play to result in an overall detriment to performance. These may include charge trapping or Dexter transfer to the slow-RISC MR-TADF dopant, although these processes have proven to be incredibly challenging to even quantify by traditional means.[70] Therefore while the improvement in colour coordinate offered by the MR-TADF hyperfluorescence strategy is welcomed, it is clear that a deeper understanding of the relevant *in operando* mechanism and processes is required to unlock their full potential.

## Conclusions

We have designed and investigated an MR-TADF compound that does not contain any explicit electron-acceptor units, opening a new design paradigm for MR-TADF emitters. SCS-CC2 calculations guided the design, confirming a strategy to coincidentally decrease $\Delta E_{ST}$ and improve oscillator strength with increasing electronic delocalization. Photophysical measurements revealed a reduced $\Delta E_{ST}$ and increased $\Phi_{PL}$ were observed in both solution and doped films for **DiICzMes$_4$** compared to **ICz** and **ICzMes$_3$**. Although $\Delta E_{ST}$ was rather large at 0.26 eV in mCP, TADF was nonetheless observed in this and other solid-state hosts. Activation of TADF occurs through the involvement of higher-lying triplet states of different orbital types to S$_1$, resulting in non-negligible SOC.[42,43] Owing to inefficient RISC, simple guest–host OLEDs showed low efficiency, although hyperfluorescent devices achieved good EQE$_{max}$ of 16.5%, at deep-blue colour coordinates (0.15, 0.11) with improved relative efficiency roll-off. Discovery of new regions of chemical space suitable for the development of MR-TADF emitters thus opens new paths towards understanding their optical properties and improving their performance.

## Conflicts of interest

There are no conflicts to declare.

## Acknowledgements

# References

1 S. Madayanad Suresh, D. Hall, D. Beljonne, Y. Olivier and E. Zysman-Colman, *Adv. Funct. Mater.*, 2020, **30**, 1908677.

2 M. Y. Wong and E. Zysman-Colman, *Adv. Mater.*, 2017, **29**, 1605444.

3 Y. Liu, C. Li, Z. Ren, S. Yan and M. R. Bryce, *Nat. Rev. Mater.*, 2018, **3**, 18020.

4 Z. Yang, Z. Mao, Z. Xie, Y. Zhang, S. Liu, J. Zhao, J. Xu, Z. Chi and M. P. Aldred, *Chem. Soc. Rev.*, 2017, **46**, 915.

5 F. Ni, N. Li, L. Zhan and C. Yang, *Adv. Opt. Mater.*, 2020, **8**, 1902187.

6 W. Chen and F. Song, *Chin. Chem. Lett.*, 2019, **30**, 1717.

7 M. A. Bryden and E. Zysman-Colman, *Chem. Soc. Rev.*, 2021, **50**, 7587.

8 C. Adachi and S. D. Sandanayaka Atula, *CCS Chem.*, 2020, **2**, 1203.

9 M. K. Etherington, J. Gibson, H. F. Higginbotham, T. J. Penfold and A. P. Monkman, *Nat. Commun.*, 2016, **7**, 13680.

10 I. A. Wright, A. Danos, S. Montanaro, A. S. Batsanov, A. P. Monkman and M. R. Bryce, *Chemistry*, 2021, **27**, 6545.

11 A. Pershin, D. Hall, V. Lemaur, J.-C. Sancho-Garcia, L. Muccioli, E. Zysman-Colman, D. Beljonne and Y. Olivier, *Nat. Commun.*, 2019, **10**, 597.

12 X. Qiu, G. Tian, C. Lin, Y. Pan, X. Ye, B. Wang, D. Ma, D. Hu, Y. Luo and Y. Ma, *Adv. Opt. Mater.*, 2020, **9**, 2001845.

13 T. Hatakeyama, K. Shiren, K. Nakajima, S. Nomura, S. Nakatsuka, K. Kinoshita, J. Ni, Y. Ono and T. Ikuta, *Adv. Mater.*, 2016, **28**, 2777.

14 P. Stachelek, J. S. Ward, P. L. Dos Santos, A. Danos, M. Colella, N. Haase, S. J. Raynes, A. S. Batsanov, M. R. Bryce and A. P. Monkman, *ACS Appl. Mater. Interfaces*, 2019, **11**, 27125.

15 Y. Wada, H. Nakagawa, S. Matsumoto, Y. Wakisaka and H. Kaji, *Nat. Photonics*, 2020, **14**, 643.

16 E. Zysman-Colman, *Nat. Photonics*, 2020, **14**, 593.

17 L.-S. Cui, A. J. Gillett, S.-F. Zhang, H. Ye, Y. Liu, X.-K. Chen, Z.-S. Lin, E. W. Evans, W. K. Myers, T. K. Ronson, H. Nakanotani, S. Reineke, J.-L. Bredas, C. Adachi and R. H. Friend, *Nat. Photonics*, 2020, **14**, 636.

18 N. Ikeda, S. Oda, R. Matsumoto, M. Yoshioka, D. Fukushima, K. Yoshiura, N. Yasuda and T. Hatakeyama, *Adv. Mater.*, 2020, **32**, e2004072.

19 K. Matsui, S. Oda, K. Yoshiura, K. Nakajima, N. Yasuda and T. Hatakeyama, *J. Am. Chem. Soc.*, 2018, **140**, 1195.

20 S. Oda, B. Kawakami, R. Kawasumi, R. Okita and T. Hatakeyama, *Org. Lett.*, 2019, **21**, 9311.

21 Y. Kondo, K. Yoshiura, S. Kitera, H. Nishi, S. Oda, H. Gotoh, Y. Sasada, M. Yanai and T. Hatakeyama, *Nat. Photonics*, 2019, **13**, 678.

22 C.-Y. Chan, M. Tanaka, Y.-T. Lee, Y.-W. Wong, H. Nakanotani, T. Hatakeyama and C. Adachi, *Nat. Photonics*, 2021, **15**, 203.

23 Y. Zhang, D. Zhang, J. Wei, Z. Liu, Y. Lu and L. Duan, *Angew. Chem., Int. Ed.*, 2019, **58**, 16912.

24 Y. T. Lee, C. Y. Chan, M. Tanaka, M. Mamada, U. Balijapalli, Y. Tsuchiya, H. Nakanotani, T. Hatakeyama and C. Adachi, *Adv. Electrode Mater.*, 2021, **7**, 2001090.

25 Y. Xu, Z. Cheng, Z. Li, B. Liang, J. Wang, J. Wei, Z. Zhang and Y. Wang, *Adv. Opt. Mater.*, 2020, **8**, 1902142.

26 S. Oda, W. Kumano, T. Hama, R. Kawasumi, K. Yoshiura and T. Hatakeyama, *Angew. Chem., Int. Ed.*, 2021, **60**, 2882.

27 Y. Xu, C. Li, Z. Li, Q. Wang, X. Cai, J. Wei and Y. Wang, *Angew. Chem., Int. Ed.*, 2020, **59**, 17442.

28 Y. Zhang, D. Zhang, J. Wei, X. Hong, Y. Lu, D. Hu, G. Li, Z. Liu, Y. Chen and L. Duan, *Angew. Chem., Int. Ed.*, 2020, **59**, 17499.

29 M. Yang, I. S. Park and T. Yasuda, *J. Am. Chem. Soc.*, 2020, **142**, 19468.

30 Y. Zhang, D. Zhang, T. Huang, A. J. Gillett, Y. Liu, D. Hu, L. Cui, Z. Bin, G. Li, J. Wei and L. Duan, *Angew. Chem., Int. Ed.*, 2021, **60**, 2049.

31 X. Cai, Y. Xu, Q. Wang, C. Li and Y. Wang, ChemRxiv. Preprint, 2021, DOI: 10.26434/chemrxiv.14371073.v1.

32 C. Li, Y. Wang, Y. Xu, Z. Li, J. Wang, J. Xue, Q. Wang and X. Cai, 2021, ChemRxiv. Preprint, DOI: 10.26434/chemrxiv.14050712.v1.

33 D. Hall, S. M. Suresh, P. L. dos Santos, E. Duda, S. Bagnich, A. Pershin, P. Rajamalli, D. B. Cordes, A. M. Z. Slawin, D. Beljonne, A. Köhler, I. D. W. Samuel, Y. Olivier and E. Zysman-Colman, *Adv. Opt. Mater.*, 2020, **8**, 1901627.

34 Y. Yuan, X. Tang, X. Y. Du, Y. Hu, Y. J. Yu, Z. Q. Jiang, L. S. Liao and S. T. Lee, *Adv. Opt. Mater.*, 2019, **7**, 1801536.

35 E. Hamzehpoor and D. F. Perepichka, *Angew. Chem., Int. Ed.*, 2020, **59**, 9977.

36 K. Wang, X.-C. Fan, Y. Tsuchiya, Y.-Z. Shi, M. Tanaka, Z. Lin, Y.-T. Lee, X. Zhang, W. Liu, G.-L. Dai, J. Chen, B. Wu, J. Zhong, J.-Y. Yuan, C.-J. Zheng, J. Yu, C. Lee, C. Adachi and X.-H. Zhang, ChemRxiv. Preprint, 2021, DOI: 10.26434/chemrxiv.13699057.v1.

37 H. Min, I. S. Park and T. Yasuda, *Angew. Chem., Int. Ed.*, 2021, **60**, 7643.

38 M. Nagata, H. Min, E. Watanabe, H. Fukumoto, Y. Mizuhata, N. Tokitoh, T. Agou and T. Yasuda, *Angew. Chem., Int. Ed.*, 2021, **60**, 20820.

39 N. Haase, A. Danos, C. Pflumm, A. Morherr, P. Stachelek, A. Mekic, W. Brütting and A. P. Monkman, *J. Phys. Chem. C*, 2018, **122**, 29173.

40 Y. Tsuchiya, S. Diesing, F. Bencheikh, Y. Wada, P. L. dos Santos, H. Kaji, E. Zysman-Colman, I. D. W. Samuel and C. Adachi, *J. Phys. Chem. A*, 2021, **125**, 8074–8089.

41 T. Serevicius, R. Skaisgiris, G. Kreiza, J. Dodonova, K. Kazlauskas, E. Orentas, S. Tumkevicius and S. Jursenas, *J. Phys. Chem. A*, 2021, **125**, 1637.

42 T. Northey and T. J. Penfold, *Org. Electron.*, 2018, **59**, 45.

43 K. Stavrou, A. Danos, T. Hama, T. Hatakeyama and A. Monkman, *ACS Appl. Mater. Interfaces*, 2021, **13**, 8643.

44 Y. Olivier, B. Yurash, L. Muccioli, G. D'Avino, O. Mikhnenko, J. C. Sancho-García, C. Adachi, T. Q. Nguyen and D. Beljonne, *Phys. Rev. Mater.*, 2017, **1**, 075602.

45 D. Sun, S. M. Suresh, D. Hall, M. Zhang, C. Si, D. B. Cordes, A. M. Z. Slawin, Y. Olivier, X. Zhang and E. Zysman-Colman, *Mater. Chem. Front.*, 2020, **4**, 2018.

46 J. A. Knoller, G. Meng, X. Wang, D. Hall, A. Pershin, D. Beljonne, Y. Olivier, S. Laschat, E. Zysman-Colman and S. Wang, *Angew. Chem., Int. Ed.*, 2020, **59**, 3156.

47 S. M. Suresh, E. Duda, D. Hall, Z. Yao, S. Bagnich, A. M. Z. Slawin, H. Bassler, D. Beljonne, M. Buck, Y. Olivier, A. Kohler and E. Zysman-Colman, *J. Am. Chem. Soc.*, 2020, **142**, 6588.

48 J. Wei, C. Zhang, D. Zhang, Y. Zhang, Z. Liu, Z. Li, G. Yu and L. Duan, *Angew. Chem., Int. Ed.*, 2021, **60**, 12269.

49 T. Taniguchi, Y. Itai, Y. Nishii, N. Tohnai and M. Miura, *Chem. Lett.*, 2019, **48**, 1160.

50 V. V. Patil, H. L. Lee, I. Kim, K. H. Lee, W. J. Chung, J. Kim, S. Park, H. Choi, W. J. Son, S. O. Jeon and J. Y. Lee, *Adv. Sci.*, 2021, e2101137.

51 P. Pander, R. Motyka, P. Zassowski, M. K. Etherington, D. Varsano, T. J. da Silva, M. J. Caldas, P. Data and A. P. Monkman, *J. Phys. Chem. C*, 2018, **122**, 23934.

52 J. A. Seo, Y. Im, S. H. Han, C. W. Lee and J. Y. Lee, *ACS Appl. Mater. Interfaces*, 2017, **9**, 37864.

53 D. G. Congrave, B. H. Drummond, V. Gray, A. D. Bond, A. Rao, R. H. Friend and H. Bronstein, *Polym. Chem.*, 2021, **12**, 1830.

54 E. Aksoy, A. Danos, C. Li, A. P. Monkman and C. Varlikli, *J. Phys. Chem. C*, 2021, **125**, 13041.

55 C. Maeda, T. Todaka and T. Ema, *Org. Lett.*, 2015, **17**, 3090.

56 S. I. Wharton, J. B. Henry, H. McNab and A. R. Mount, *Chem. – Eur. J.*, 2009, **15**, 5482.

57 K. Karon and M. Lapkowski, *J. Solid State Electrochem.*, 2015, **19**, 2601.

58 N. G. Connelly and W. E. Geiger, *Chem. Rev.*, 1996, **96**, 877.

59 C. M. Cardona, W. Li, A. E. Kaifer, D. Stockdale and G. C. Bazan, *Adv. Mater.*, 2011, **23**, 2367.

60 S. H. Kim, J. Jang and J. Y. Lee, *Appl. Phys. Lett.*, 2007, **90**, 223505.

61 J. S. Ward, R. S. Nobuyasu, A. S. Batsanov, P. Data, A. P. Monkman, F. B. Dias and M. R. Bryce, *Chem. Commun.*, 2016, **52**, 2612.

62 F. B. Dias, T. J. Penfold and A. P. Monkman, *Methods Appl. Fluoresc.*, 2017, **5**, 012001.

63 K. Masui, H. Nakanotani and C. Adachi, *Org. Electron.*, 2013, **14**, 2721.

64 V. V. Patil, J. Lim and J. Y. Lee, *ACS Appl. Mater. Interfaces*, 2021, **13**, 14440.

65 H. L. Lee, W. J. Chung and J. Y. Lee, *Small*, 2020, **16**, e1907569.

66 D. Zhang, X. Song, A. J. Gillett, B. H. Drummond, S. T. E. Jones, G. Li, H. He, M. Cai, D. Credgington and L. Duan, *Adv. Mater.*, 2020, **32**, e1908355.

67 S. H. Han, J. H. Jeong, J. W. Yoo and J. Y. Lee, *J. Mater. Chem. C*, 2019, **7**, 3082.

68 S. O. Jeon, K. H. Lee, J. S. Kim, S.-G. Ihn, Y. S. Chung, J. W. Kim, H. Lee, S. Kim, H. Choi and J. Y. Lee, *Nat. Photonics*, 2021, **15**, 208.

69 A. Monkman, *ACS Appl. Mater. Interfaces*, 2021.

70 N. Haase, A. Danos, C. Pflumm, P. Stachelek, W. Brütting and A. P. Monkman, *Mater. Horiz.*, 2021, **8**, 1805.